Design Principles for High-Performance Meta-Polybenzimidazole Membranes for Vanadium Redox Flow Batteries

RESEARCH ARTICLE

Renewable Energy

Energy & Environmental Materials WILEY

Design Principles for High-Performance *Meta*-Polybenzimidazole Membranes for Vanadium Redox Flow Batteries

*Jacobus C. Duburg, Jonathan Avaro, Leonard Krupnik, Bruno F.B. Silva, Antonia Neels, Thomas J. Schmidt, and Lorenz Gubler**

The all-vanadium redox flow battery (VRFB) plays an important role in the energy transition toward renewable technologies by providing grid-scale energy storage. Their deployment, however, is limited by the lack of membranes that provide both a high energy efficiency and capacity retention. Typically, the improvement of the battery's energy efficiency comes at the cost of its capacity retention. Herein, novel N-alkylated and N-benzylated *meta*-polybenzimidazole (*m*-PBI) membranes are used to understand the molecular requirements of the polymer electrolyte in a vanadium redox flow battery, providing an important toolbox for future research toward next-generation membrane materials in energy storage devices. The addition of an ethyl side chain to the *m*-PBI backbone increases its affinity toward the acidic electrolyte, thereby increasing its ionic conductivity and the corresponding energy efficiency of the VRFB cell from 70% to 78% at a current density of 200 mA cm^{-2}. In addition, cells equipped with ethylated *m*-PBI showed better capacity retention than their pristine counterpart, respectively 91% versus 87%, over 200 cycles at 200 mA cm^{-2}. The outstanding VRFB cycling performance, together with the low-cost and fluorine-free chemistry of the N-alkylated *m*-PBI polymer, makes this material a promising membrane to be used in next-generation VRFB systems.

1. Introduction

The transition from a fossil fuel-based society to a society based on renewable energy is one of the biggest challenges of the 21st century. Herein, the incorporation of renewable energy generation technologies, such as solar or wind, into a global energy network is limited by the inherent intermittent nature of power generation.[1] This requires the use of energy storage technologies to adjust the energy output to its demand at any given time.[2] Energy storage technologies can be characterized according to their capacity, storage duration, and longevity of operation in terms of cycle life.[2] In the category for intermediate to long-term storage (daily to weekly discharge), redox flow batteries (RFBs) are promising candidates for energy storage due to their unique architecture, consisting of the electrochemical conversion unit and external electrolyte-containing storage tanks, therefore enabling the independent scalability of nominal power and energy capacity.[2–4]

RFB technologies can be further distinguished according to the chemistry of the redox couples, ranging from organic RFBs, metal-ion-based RFBs, and gas-containing systems.[5–9] Currently, the most industrially advanced RFB system is the all-vanadium redox flow battery, with a V^{2+}/V^{3+} redox couple on the negative electrode and a VO_2^+/VO^{2+} redox couple on the positive electrode.[10,11] The electroactive vanadium species are dissolved in an acidic electrolyte that enables the electrochemical reactions by supplying water and protons to the system. Nowadays, VRFB systems are commonly equipped with a perfluoroalkylsulfonic acid (PFSA) membrane of the Nafion™-type or fluorinated anion exchange membranes (Fumatech FAP series).[12,13] Although PFSA membranes offer excellent ionic conductivity and chemical stability, they suffer from their high cost and significant capacity fading.[14,15] The severe capacity loss can be attributed to a greater asymmetric vanadium and electrolyte flux during charging and discharging, as described in earlier work by Oldenburg et al.,[16] resulting in a net vanadium flux toward the positive electrode and, as such, a loss of vanadium in the anolyte. On the contrary, a net vanadium flux toward the anolyte is observed for anion exchange membranes (AEMs).[16] A follow-up study by Oldenburg et al.[17] showed that the net vanadium flux can be reduced by

J. C. Duburg, Prof. Dr. T. J. Schmidt, Dr. L. Gubler
Center for Energy and Environmental Sciences, Paul Scherrer Institut, Forschungsstrasse 111, Villigen PSI 5232, Switzerland
E-mail: lorenz.gubler@psi.ch
Dr. J. Avaro, L. Krupnik, Dr. B. F. B. Silva, Prof. Dr. A. Neels
Empa, Swiss Federal Laboratories for Materials Science and Technology, Center for X-ray Analytics, Lerchenfeldstrasse 5, 9014, St. Gallen, Switzerland
Dr. J. Avaro, Dr. B. F. B. Silva
Empa, Swiss Federal Laboratories for Materials Science and Technology, Laboratory for Biomimetic Membranes and Textiles, Lerchenfeldstrasse 5, 9014, St. Gallen, Switzerland
L. Krupnik, Prof. Dr. A. Neels
Department of Chemistry, University of Fribourg, Chemin du Musée 9, 1700, Fribourg, Switzerland
Dr. B. F. B. Silva
Empa, Swiss Federal Laboratories for Materials Science and Technology, Laboratory for Biointerfaces, Lerchenfeldstrasse 5, 9014, St. Gallen, Switzerland
Prof. Dr. T. J. Schmidt
Institute of Molecular Physical Science, ETH Zurich, 8093, Zurich, Switzerland
The ORCID identification number(s) for the author(s) of this article can be found under https://doi.org/10.1002/eem2.12793.

DOI: 10.1002/eem2.12793

combining both membrane types to form an amphoteric polybenzimidazole-Nafion™ bilayer membrane. Although the capacity fading of PFSA membranes can be mitigated in this fashion, their high cost remains an issue.[12,14]

With this in mind, novel hydrocarbon-based anion exchange membranes based on pyridine or imidazole moieties sparked the attention of the scientific community.[15,18–21] One of these polymers, polybenzimidazole (PBI), was already shown to exhibit interesting properties for high-temperature polymer electrolyte fuel cells (HT-PEFCs) in the early 2000s due to its excellent mechanical and chemical stability.[22–24] Currently, the use of PBI in HT-PEFCs is at a commercial level, making PBI a widely available polymer that can be easily adapted to other devices, such as a VRFB, where it has been shown to be stable for 13 500 cycles.[25] Furthermore, its cost is only a fraction of that of Nafion™, with the *meta*-PBI (m-PBI) variant being seven times less expensive.[26] Taking into consideration the lower thickness requirement for m-PBI membranes, this cost reduction increases to 97% compared to its PFSA counterpart.[26]

PBI, in its pristine state, is an insulator. However, it develops the characteristics of an anion exchange membrane upon the protonation of the benzimidazole moiety (5.6 pK_{aH}) by an acidic electrolyte, giving rise to an ionic conductivity of ~5 mS cm^{-1} in 2 M H_2SO_4, which can mainly be attributed to the transport of protons as demonstrated by Dai et al.[27–29] Unfortunately, due to the dense polymer packing of the PBI backbone,[15,30] this conductivity is significantly lower than that of Nafion™, 92 ± 4 mS cm^{-1}, resulting in a high ohmic drop across the membrane during operation.

Several solutions were proposed to reduce the ohmic resistance of PBI membranes and therefore increase their effectiveness in VRFBs.[18,31,32] Yuan et al.[25] put forward the use of a sponge-like porous O-PBI membrane equipped with micron-sized cells separated by positively charged walls. The microstructure obtained herein enhanced the selectivity toward H^+ while also maintaining excellent conductivity, giving rise to an energy efficiency of 78% at 200 mA cm^{-2}, thereby outperforming Nafion™ N115.

Noh et al.[27] proposed the addition of an alkaline preswelling step, thereby opening up the microstructure of the m-PBI membrane and, as such, increasing its electrolyte uptake. The biggest improvement in selectivity in terms of ionic conductivity and VO^{2+} diffusion was observed for membranes preswollen in 4 M NaOH, with a measured energy efficiency of 91.3% at 80 mA cm^{-2}.

Another approach proposed by our research group showed the performance of m-PBI membranes to be greatly improved by laminating a thin m-PBI skin layer, providing transport selectivity, onto a porous separator, thereby evading the mechanical issues that arise for thin membranes.[33] A follow-up study showed that a composite membrane, comprising a 6 µm m-PBI skin layer laminated onto a 30 µm polypropylene support, was able to outperform Nafion™ NR212 in terms of energy efficiency at 120 mA cm^{-2} (84% and 82%, respectively), while exhibiting a 99% capacity retention over 90 cycles.[34]

So far, all the listed approaches concern the processing of the PBI membrane to increase its conductivity. However, another option is to improve the inherent conductivity of the dense polymer electrolyte itself through the chemical modification of the PBI backbone.[15,32,35–38] Side chains attached to the PBI backbone can be categorized into two types: ionic and nonionic. Yan et al.[39] introduced a sulfonic acid-terminated side chain onto an O-PBI backbone, thereby enabling the formation of a 55 µm thick membrane that outperforms Nafion™ NR212 in both efficiency and capacity retention. Jang et al. chose the nonionic approach by grafting a 3-methylbutane side chain onto an ABPBI polymer backbone. The addition of this alkyl spacer enhanced the acid absorption of the membrane and, thereby, its conductivity in acidic media. Although all of these approaches saw a significant boost in the cell performance of the polymer electrolyte, the system tended to suffer from increased capacity fading due to their more open structure or reduced Donnan exclusion toward the positively charged vanadium species, a feature that is the most compelling reason for PBI equipped VRFB systems.

This work describes the synthesis of novel N-alkylated and N-benzylated m-PBI derivatives while forming a fundamental understanding of the correlation between the molecular structure and the ionic conductivity, mechanical stability, and vanadium barrier properties of the polymer electrolyte. The addition of small nonionic alkyl side chains alters the packing of the m-PBI backbone, forming a less ordered structure, thereby increasing the electrolyte content inside the membrane and, as such, the performance of the VRFB system. Additionally, the low cost of the fluorine-free and easily accessible m-PBI precursor, together with the increased performance and identically low capacity fading of the alkylated m-PBI polymer electrolyte, makes this class of membranes a promising candidate for next-generation materials to be used in flow battery applications.

2. Results and Discussion

Functionalized m-PBI derivatives containing small alkyl and benzyl pendant chains were synthesized through the deprotonation of the N-H moiety, followed by the addition of a commercially available halogenated reagent (**Figure 1**; Table S1, Supporting Information).

Model compounds with an envisaged degree of functionalization (DoF) of 50% were prepared to study the influence of the respective side chains on the performance of the membrane. m-PBI derivatives showing promising ex situ properties in terms of ionic conductivity and acid uptake were further analyzed through the synthesis of derivatives with a 100% DoF.

The chemical structure of the functionalized polymers was analyzed by ^{1}H NMR in DMSO-d_6. The NMR spectra (Figures S1–S9, Supporting Information) of the alkylated derivatives show a reduction of the N-H signal at 13.2 ppm, with new peaks forming in the aliphatic region, indicating the successful addition of alkyl chains to the m-PBI backbone. In contrast, the benzylated materials show a new peak forming at 5.7 ppm, belonging to the protons of the CH_2 group between the aromatic m-PBI backbone and the benzyl moiety of the attached pendant group. The DoFs of the m-PBI derivatives were derived from the ratio between the newly formed signals and those of the m-PBI backbone as described in the Section 4 for the synthesis of functionalized PBI (**Table 1**).

All functionalized m-PBI polymers show a slightly higher DoF, respectively ~60%, than the aimed for 50%, attributed to the presence of residual N,N-dimethylacetamide (DMAc) present in the pristine m-PBI material, resulting in an overestimation of the m-PBI molar quantity.

Membranes were prepared through the dissolution of the polymer, 15 wt.% of the m-PBI backbone, in DMAc, followed by a solution casting process with a fixed blade gap and a solvent evaporation step (Membrane preparation). Membranes with a dry thickness of 18–22 µm were used for ex situ characterization, with 12–15 µm membranes being subjected to in situ cell testing (**Figure 2**).

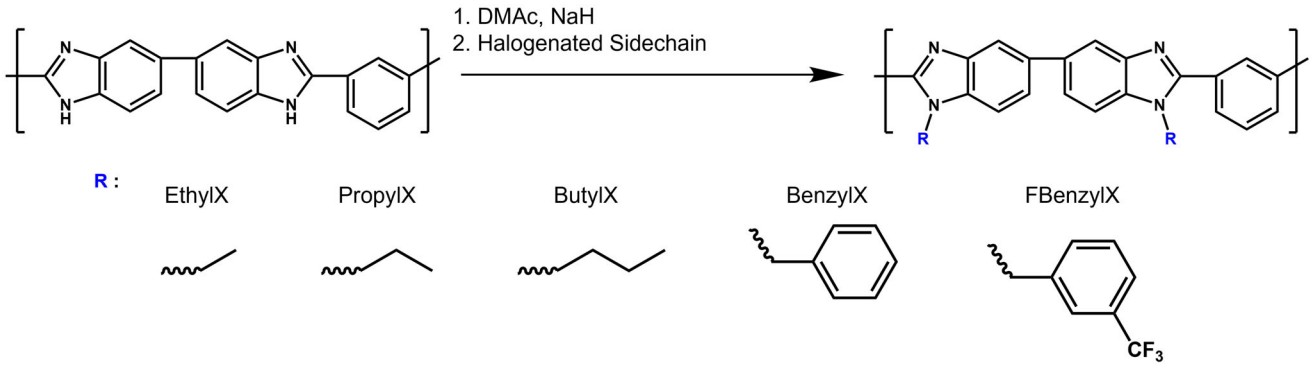

Figure 1. Schematic representation of the synthesis of *m*-PBI derivatives through the deprotonation with NaH, followed by an alkylation or benzylation step.

Table 1. Degree of functionalization of *m*-PBI derivatives as measured with ^{1}H NMR.

Polymer name	Alkyl/Benzyl signal	Aromatic signals	Degree of functionalization (%)
Ethyl63	3.79	10.0	63
Ethyl100	6.04	10.0	100
Propyl60	3.62	10.0	60
Propyl100	6.01	10.0	100
Butyl55	3.30	10.0	55
Benzyl59	2.36	15.9	59
FBenzyl56	2.26	14.5	56

The properties of the newly prepared m-PBI polymers in acidic media were studied through the dimensional swelling in the thickness direction, ionic conductivity, and mass uptake in 2 M H_2SO_4. Here, the mass uptake was divided into the water and sulfuric acid fractions inside the membrane, with the acid doping level (ADL) of the membrane being calculated from the latter (Equation 9).

The behavior of the membrane in acidic media changes significantly upon alkylation or benzylation of the m-PBI backbone, with a distinct difference between the two types of modified materials and their pristine counterparts (**Figure 3**). Whereas benzylated membranes show a drop in both the thickness of swelling and ionic conductivity, alkylation improves these features. Furthermore, within the alkylated polymers, the membrane's ionic conductivity decreases with increasing length of the alkyl chain, from 12.8 ± 0.5 mS cm^{-1} for Ethyl63 to 7.9 ± 0.2 mS cm^{-1} for Butyl55. Following this trend, even higher conductivity can be expected for methylated m-PBI derivatives. However, this specific chemical modification is not part of the present work and remains a prospective research topic. A further improvement in conductivity was obtained by increasing the DoF to 100%, respectively, 24.5 ± 1.7 mS cm^{-1} for Ethyl100 and 23.4 ± 0.8 mS cm^{-1} for Propyl100. Nonetheless, the conductivity in 2 M H_2SO_4 remains lower than that of Nafion™ NR212, 92.1 ± 3.9 mS cm^{-1}.

A similar trend as the ionic conductivity in 2 M H_2SO_4 can be seen for the mass uptake and corresponding ADL of the functionalized materials in this solution. Here, the sulfuric acid fraction inside the membrane was shown to increase for ethylated and propylated derivatives, therefore increasing the ADL of the membrane. Although the butylated membrane did not show an increase in mass uptake, the ADL increased due to its higher molar mass. These observations suggest that introducing short alkyl chains into the polymer backbone alters the polymer packing, rendering it more amorphous (cf. the structural analysis below for further details), as also observed by Jang et al.[40] with the introduction of an isopentyl spacer to an ABPBI backbone, leading to improved membrane properties in acidic media. The drop in conductivity and swelling within this group (alkylated polymers) could be attributed to the increasing hydrophobicity with increasing alkyl chain length. Conversely, benzylation leads to a decline in membrane properties, evidenced by a lowered thickness swelling, mass uptake, and ADL, attributed to the more hydrophobic nature of the material, in addition to the stronger interactions between the polymer chains (Figure S10, Supporting Information).

Alongside the swelling and electrolyte uptake properties of the membrane in the acidic electrolyte, the membranes also need to be

Figure 2. a) 19 µm *m*-PBI membrane on glass, b) free-standing 14 µm *m*-PBI membrane, and c) 13 µm Ethyl63 membrane after 200 cycles at 200 mA cm^{-2}.

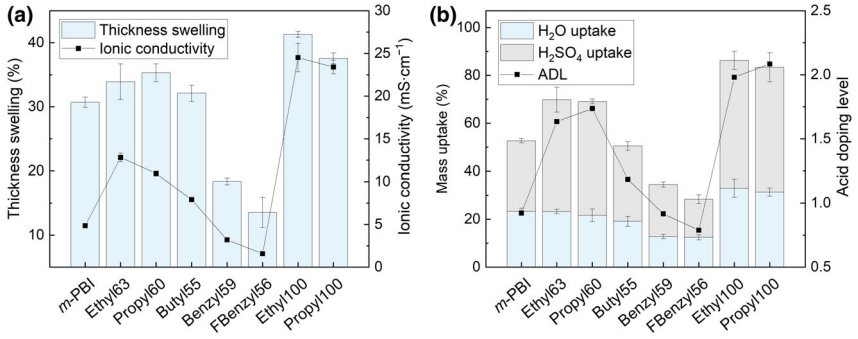

Figure 3. Ex situ properties of *m*-PBI derivatives in 2 M H_2SO_4, a) thickness swelling, ionic conductivity, b) mass uptake, and acid doping level (ADL).

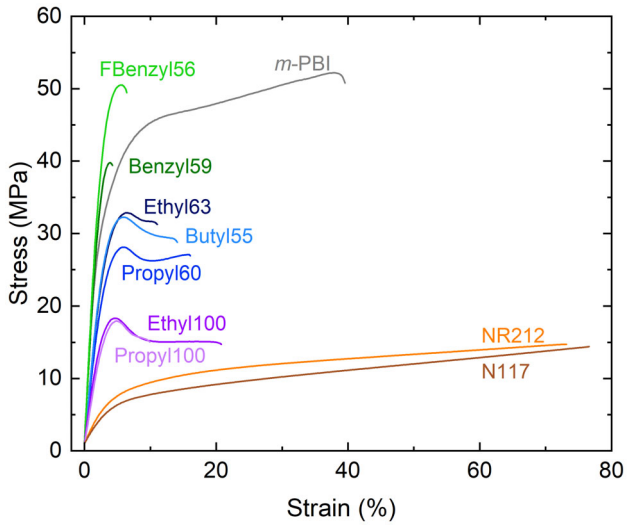

Figure 4. Stress-strain diagram of 2 M H_2SO_4-swollen N-alkylated and N-benzylated materials with Nafion™ N117, NR212, and *m*-PBI as references.

Table 2. VO^{2+} barrier properties of *m*-PBI, Nafion™ NR212, and N-alkylated *m*-PBI.

Polymer name	Slope (mol L^{-1} h^{-1})	VO^{2+} Diffusion Coefficient (cm^2 min^{-1})	Ratio versus *m*-PBI
m-PBI	$(1.05 \pm 0.03)\cdot10^{-6}$	$(1.6 \pm 0.1)\cdot10^{-10}$	–
NR212	$(2.30 \pm 0.03)\cdot10^{-3}$	$(110.9 \pm 1.3)\cdot10^{-8}$	$6.8\cdot10^{3}$
Ethyl63	$(3.65 \pm 0.04)\cdot10^{-5}$	$(83.6 \pm 0.8)\cdot10^{-10}$	51
Ethyl100	$(1.20 \pm 0.01)\cdot10^{-4}$	$(283.8 \pm 2.2)\cdot10^{-10}$	$1.7\cdot10^{2}$
Propyl60	$(1.13 \pm 0.03)\cdot10^{-5}$	$(27.6 \pm 0.6)\cdot10^{-10}$	17
Propyl100	$(6.71 \pm 0.12)\cdot10^{-5}$	$(130.5 \pm 2.4)\cdot10^{-10}$	80
Butyl55	$(3.11 \pm 0.06)\cdot10^{-6}$	$(5.5 \pm 0.1)\cdot10^{-10}$	3.4

mechanically robust for handling purposes and cell operation. The mechanical strength of the newly prepared PBI derivatives in 2 M H_2SO_4 was assessed through a tensile strength testing procedure (Mechanical strength) (**Figure 4**). Again, a clear distinction can be made between the alkylated and benzylated materials, with the latter being able to withstand a higher stress before breaking. In comparison with its pristine counterpart, the benzylated materials are able to withstand a similar stress while exhibiting a reduced strain, giving them a larger Young's modulus (Table S4, Supporting Information). Alkylated materials, on the other hand, show a reduced tensile strength compared to m-PBI, with 28–32 MPa for the partially functionalized materials, compared to 54 ± 10 MPa for m-PBI, and a lower Young's modulus. A further reduction in mechanical strength, to a tensile strength of ~18 MPa, is observed for the fully alkylated materials, Ethyl100 and Propyl100. Although Nafion™-type membranes are only able to withstand a stress of 15 MPa, they can be used at a larger thickness due to their high ionic conductivity, providing them with the necessary mechanical robustness.

Another key feature is the membrane's ability to act as a barrier toward the electroactive vanadium species. The VO^{2+} diffusion through the alkylated membranes was assessed in a home-built diffusion cell (Figure S16, Supporting Information). Benzylated membranes were excluded from testing due to their poor ADL and corresponding ionic conductivity, as depicted in Figure 3. The VO^{2+} diffusivity through the membranes shows a similar trend as the ionic conductivity (**Table 2**, **Figure 5**), shown in Figure 3. The addition of smaller alkyl chains to the m-PBI backbone leads to a higher crossover of VO^{2+} species, increasing from $(5.5 \pm 0.1)\cdot10^{-10}$ cm^2 min^{-1} for Butyl55 to $(27.6 \pm 0.6)\cdot10^{-10}$ cm^2 min^{-1} for Propyl60 to $(83.6 \pm 0.8)\cdot10^{-10}$ cm^2 min^{-1} for Ethyl63. Furthermore, as was the case for the ionic conductivity, the VO^{2+} diffusion increases with increasing DoF, with a VO^{2+} diffusion coefficient of $(283.8 \pm 2.2)\cdot10^{-10}$ cm^2 min^{-1} seen for Ethyl100, roughly 3.4 times larger than those of the partially ethylated Ethyl63. Although the vanadium barrier properties of the alkylated materials decrease, they remain significantly better than that of Nafion™ NR212 with $(110.9 \pm 1.3)\cdot10^{-8}$ cm^2 min^{-1}. The difference in vanadium permeability of the m-PBI materials compared to Nafion™ NR212 can be attributed to the size of the aqueous domains inside the polymer electrolyte. These domains are substantially smaller in m-PBI due to its dense polymer packing, whereas Nafion™ membranes are known to develop large aqueous domains, which promote vanadium transport.[41,42]

Correlating the membrane VO^{2+} diffusion coefficient to their respective ionic conductivity in a vanadium electrolyte (oxidation state 3.5, **Figure 6**), a nonlinear trend is observed. The beneficial effects of m-PBI alkylation are evident in the region stretching from m-PBI to Ethyl63. This region highlights the favorable scenario where the ionic conductivity increases significantly while the VO^{2+} crossover increases only marginally. Increasing the conductivity of the membrane beyond this point results in a negative return, where a small increase in conductivity will result in a much greater increase in the VO^{2+} crossover. An optimal tradeoff between membrane conductivity and the VO^{2+} crossover is found in the transition region of the graph, where an increase in conductivity will lead to a comparable increase in the VO^{2+} crossover, as seen in the top left section of the figure. Out of the alkylated derivatives, Ethyl63 is the material closest to this optimal region, with the change from Propyl100 to Ethyl100 giving the largest negative return.

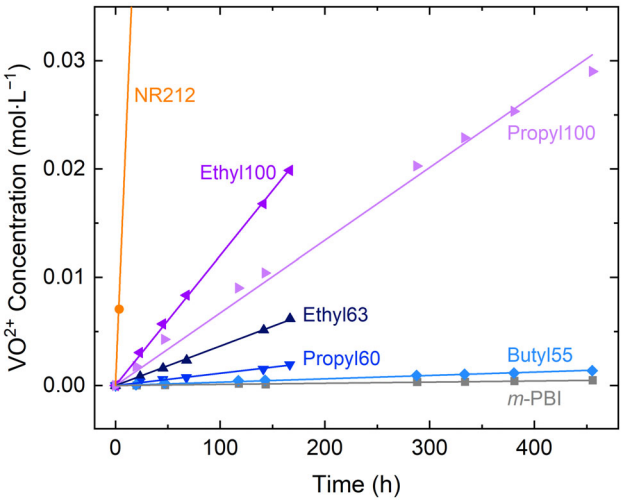

Figure 5. VO^{2+} diffusion through Nafion™ NR212, *m*-PBI, and N-alkylated *m*-PBI.

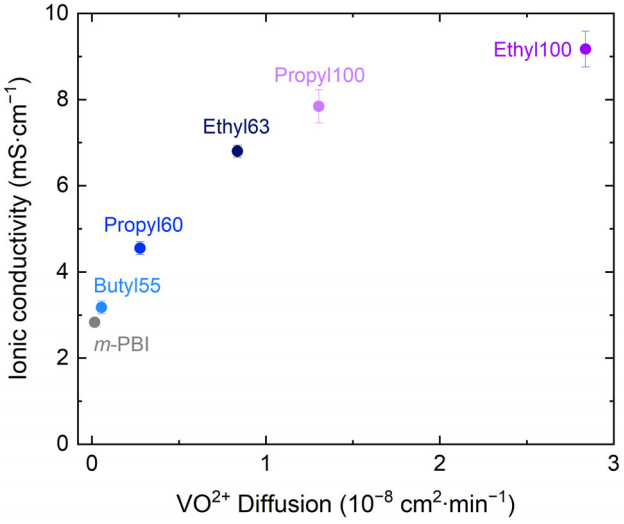

Figure 6. Ionic conductivity in the vanadium electrolyte (oxidation state 3.5) of alkylated and pristine *m*-PBI with their corresponding VO^{2+} diffusion coefficient. The ionic conductivity of benzylated derivatives can be found in Table S3, Supporting Information.

To further deepen the knowledge between the molecular structure, membrane morphology, and membrane properties and identify correlations to the observed ex situ properties, the ethylated and propylated membranes were subjected to wide-angle X-ray scattering (WAXS) in their dry state and small-angle X-ray scattering (SAXS) in their 2 M H_2SO_4 swollen form, with m-PBI acting as reference (**Figure 7**). In addition, analysis of the membranes in the dry state with SAXS and in the swollen state with WAXS was also attempted. However, these measurements did not provide the required contrast for further analysis.

In its dry state, pristine m-PBI shows two distinct features: a large peak at a 2Θ of 18.0°, corresponding to a correlation distance of 4.9 Å, and a smaller shoulder at a 2Θ of ca. 7.7°, corresponding to a correlation distance of 11.5 Å (Figure 7a,b). Upon benzylating the m-PBI polymer, the signal at 18.0° shifts to 19.6°, a correlation distance of 4.5 Å (Figure S10, Supporting Information), indicating a stronger interaction between polymer chains, which explains the reduced swelling and uptake of the benzylated m-PBI derivative. In contrast, ethylation or propylation of the m-PBI backbone gives two main features, with a peak at a 2Θ of 19–21° in addition to a newly formed peak at a 2Θ of 13–15°. The intensity of the signal at 19–21° does not change with increasing DoF and can therefore be attributed to the PBI backbone. On the other hand, the signal at 13–15° increases in intensity and shifts to lower angles with increasing DoF. As such, this signal can be attributed to the addition of the alkyl chain, showing that the polymer packing becomes less ordered, with two correlation distances seen upon alkylation. The origin of this less ordered microstructure may be ascribed to two phenomena. First, the alkyl sidechains can act as spacers, thereby hindering the conventionally seen dense polymer packing of PBI materials. In addition, the alkylation process removes the hydrogen bond donors in the benzimidazole backbone, thereby reducing the interaction strength between the polymer chains.

The change in the polymer packing upon alkylation can also be observed in its 2 M H_2SO_4 swollen state, as measured by SAXS. Here, all alkylated samples show a singular feature at a q-value of ca. 0.52 nm^{-1}, indicating structural periodicities within the swollen polymer of ca. 120 Å. These features can be related to the size of the ionic clusters of the polymer,[43] or the spacing between them (Figure 7c, d). The intensity of this signal decreases with increasing DoF for both the ethylated and propylated m-PBI, indicating that the bulk structure becomes more disordered upon alkylation, thereby explaining the higher electrolyte uptake, thickness swelling, and lower mechanical strength of the films.

For commercial viability, a VRFB cell must show a long calendar life, with all cell components being able to withstand the cycling conditions. Herein, the oxidative stability of the cell components plays an important role due to the presence of the strongly oxidizing VO_2^+ species in the charged catholyte. The oxidative stability of m-PBI and the m-PBI derivatives with improved ionic conductivity, respectively, ethylated and propylated m-PBI, was assessed in an accelerated stress test using a VO_2^+ electrolyte solution for 66 days (**Figure 8**). Here, the VO^{2+} concentration in the electrolyte, formed due to the reduction of VO_2^+ by oxidizing the polymer, was determined with UV-Vis spectroscopy after 21, 42, and 66 days (Chemical stability). The formation of VO^{2+} species was observed for all polymers, with the highest rate of formation seen in the initial 3 weeks of the experiment (Figure 8). After 3 weeks, a more linear trend of membrane degradation is seen, indicating a decrease in reactivity toward the membrane of the oxidative species. The ethylated materials, Ethyl63 and Ethyl100, experience substantially faster degradation than pristine m-PBI, with almost twice the amount of VO^{2+} formed after 66 days. On the contrary, propylation results in only a minimal increase in VO^{2+} concentration in the initial 3 weeks of the oxidative study with respect to m-PBI, with a similar extent of degradation at the end of the test. Comparing the FTIR spectra of the samples before and after the oxidative test (Figure S12, Supporting Information), a new signal is observed at 972 cm^{-1} for all samples, potentially displaying bond cleavage of the PBI backbone. The exact mechanism of this degradation is to be studied in detail. Although degradation can be observed in all samples, propylation can be considered an interesting option to improve the ionic conductivity of an m-PBI polymer without

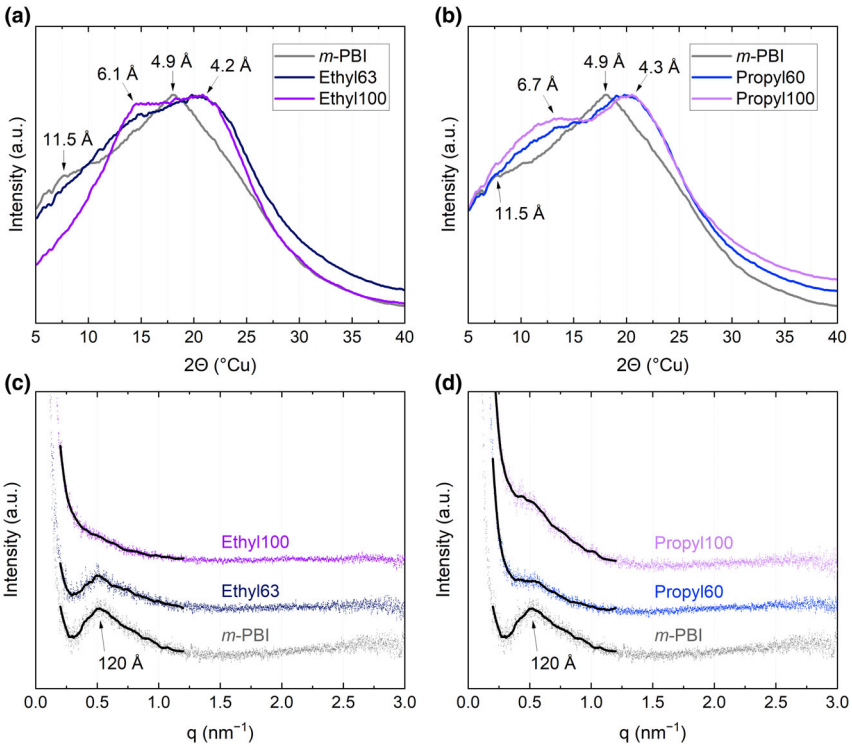

Figure 7. Transmission WAXS patterns of a) dry ethylated *m*-PBI and b) propylated *m*-PBI, and c, d) their corresponding 2 M H_2SO_4 swollen SAXS patterns in, respectively, with *m*-PBI acting as a reference. The SAXS patterns are overlaid with a smoothed fit as a visual aid, with a *q*-value of 3 nm^{-1} corresponding to a 2Θ (°Cu) of 4°.

negatively affecting its oxidative stability with respect to its pristine m-PBI counterpart.

The in situ characteristics of m-PBI derivatives with a dry thickness of 12–15 μm (**Table 3**) were assessed in a VRFB setup as described in Cell cycling. Due to a decreasing mechanical stability upon alkylation (Figure 4), fully alkylated materials, Ethyl100 and Propyl100, suffered from pinhole formation during the membrane's conditioning phase in the VRFB cell and therefore did not exhibit the required mechanical properties in this thickness range to enable cell testing. Laminating a thin film on top of a porous support providing mechanical stability, as highlighted in our earlier work, enables cell testing, yet this is considered outside the scope of this work.[33,34]

The partially functionalized polymers could be cycled without any mechanically related issues, suggesting that a mechanical strength exceeding 25 MPa for membranes with a dry thickness of 13 μm is sufficient to enable cell testing.

The resistance and corresponding overpotentials of the membrane were assessed through electrochemical impedance spectroscopy (EIS) and polarization measurements, with the resistance at a state of charge (SoC) of −50% (V^{3+} and VO^{2+} at a 1:1 ratio) and the polarization curve at a SoC of 50% being depicted in Table 3 and **Figure 9**, respectively.

Similar to what is observed in the ex situ characteristics, N-benzylated materials suffered from poor membrane conductivity due to their stronger polymer chain interactions and lower electrolyte uptake, resulting in a high area-specific resistance (ASR) of, respectively, 1.31 and 1.61 Ω cm^2 for Benzyl59 and FBenzyl56. Consequently, these materials experience a high ohmic overpotential, increasing the slope of their corresponding polarization curve. In contrast, N-alkylated derivatives exhibit a higher ionic conductivity in the vanadium electrolyte than their pristine counterpart, as seen by their reduced ASR. Furthermore, an increase in the alkyl chain length leads to an increase in the ASR, from 0.31 Ω cm^2 for Ethyl63 to 0.55 Ω cm^2 for Butyl55, with the latter only showing minimal improvement over pristine m-PBI. The increase in ASR upon increasing the alkyl chain length is attributed to the addition of the longer hydrophobic alkyl chain, reducing the electrolyte uptake and thickness swelling (Figure 3).

The cycling behavior and efficiency metrics of the cells with different membranes were assessed at current densities between 80 and 200 mA cm^{-2} (**Figure 10**). Comparing the N-alkylated materials to Nafion™ NR212 (for the benzylated derivatives, please see Figure S24, Supporting Information), a higher coulombic efficiency (CE) is observed, with all the PBI polymers exhibiting a CE close to 100%, compared to a CE of 97% for Nafion™ NR212.

The voltaic efficiency (VE) of the membranes can be seen as a direct representative of the overpotentials in the system, with the ohmic contribution being the only variable in this experiment. As such, a direct correlation with the membrane's ASR is observed, with the highest VE being observed for Ethyl63 and Nafion™ NR212, followed by Propyl60, Butyl55, and lastly m-PBI (Figure 10b). Combining the coulombic and voltaic efficiency into the overall energy efficiency (EE), the highest EE over this current density regime is measured for Ethyl63, closely followed by Propyl60, with both exceeding Nafion™ NR212 due to their superior coulombic efficiency. A much greater difference between the N-alkylated materials and Nafion™ NR212 is witnessed in discharge capacity (Figure 10d), with Nafion™ NR212 showing a substantial loss of capacity versus the minimal capacity fading of the PBI-based materials.

To improve the technical viability of commercial VRFB storage systems, they need to be able to operate at both a high current density and energy efficiency, a characteristic that is observed for both Ethyl63 and Propyl60 at a current density of 200 mA cm^{-2}, with an energy efficiency exceeding 75%. Taking this into consideration, these materials were subjected to an extended cycling test comprising 200 charge–discharge cycles at a current density of 200 mA cm^{-2} to further analyze their operational stability (**Figure 11**). Like before (Figure 10), the highest energy efficiency over 200 cycles is observed for Ethyl63 (~78%), with Propyl60 exhibiting an energy efficiency of ~76%. Although the addition of alkyl chains to the m-PBI backbone has been shown to decrease the membrane's barrier toward VO^{2+} species (Figure 5), a comparable capacity fading over 200 cycles was observed for all PBI materials. The loss of capacity, as a result of the crossover of all electroactive vanadium species at a current density of 200 mA cm^{-2}, does not show a direct correlation with the measured ex situ VO^{2+} diffusion. At this current density, a sizeable contribution of the migration-

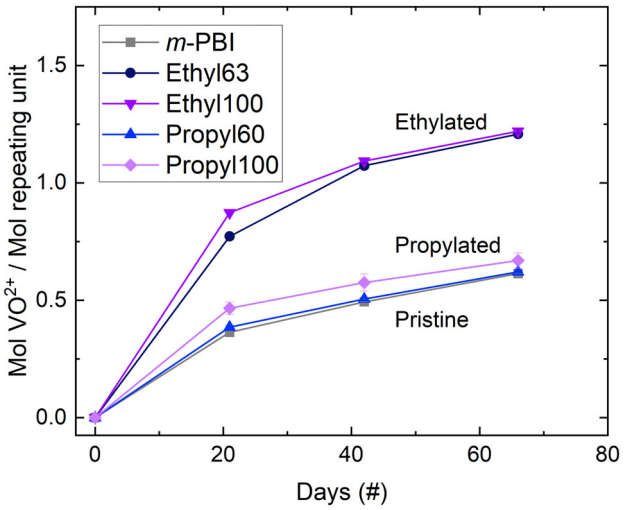

Figure 8. The VO^{2+} formation of *m*-PBI, Ethyl63, Propyl60, Ethyl100, and Propyl100 membranes after 21, 42, and 66 days as a result of an oxidizing VO_2^+ electrolyte solution.

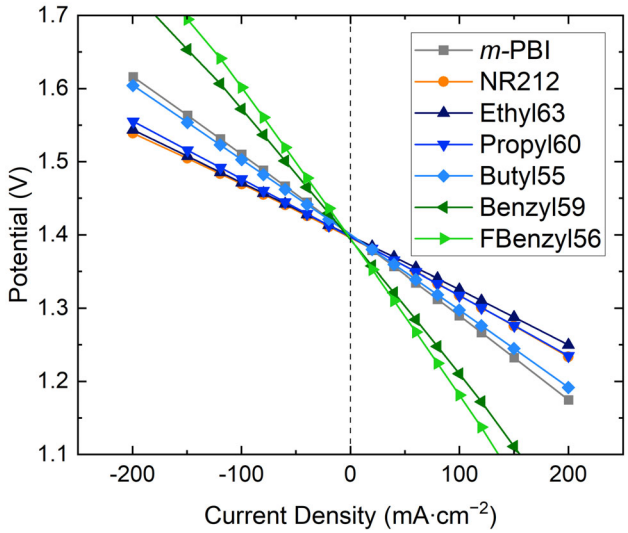

Figure 9. Non IR-corrected polarization curves of *m*-PBI, *m*-PBI derivatives, and Nafion™ NR212 at a state of charge of 50%.

Table 3. Area-specific resistance (ASR) of chemically modified *m*-PBI at a state of charge of −50%. All ASR values were corrected for the internal cell resistance, measured by stacking several NR212 layers, of $0.24 \pm 0.04\ \Omega\ cm^2$.

Membrane	Dry thickness (μm)	ASR ($\Omega\ cm^2$)
m-PBI	13.6	0.58 ± 0.04
NR212	50.8	0.28 ± 0.04
Ethyl63	12.8	0.31 ± 0.04
Propyl60	13.1	0.38 ± 0.04
Butyl55	13.3	0.55 ± 0.04
Benzyl59	14.4	1.31 ± 0.04
FBenzyl56	13.5	1.61 ± 0.04

driven vanadium flux is to be expected.[17,44] The minimal differences in capacity decay between pristine and alkylated m-PBI suggest that despite the increase in VO^{2+} crossover, the net vanadium flux at this current density remains comparable, with m-PBI having a capacity retention of 87% of its starting capacity, versus 91% and 88% for Ethyl63 and Propyl60, respectively. In addition, the reduced absolute loss of capacity for Ethyl63 of 7% with respect to the theoretical maximum versus Nafion™ NR212 and m-PBI, respectively, 48% and 8%, over these 200 cycles at 200 mA cm^{-2}, highlights that the addition of a small alkyl chain to the m-PBI backbone can boost the performance of the VRFB system without adversely affecting its capacity retention.

Although the capacity decay is unaffected by the alkyl chain addition, the crossover of the supporting electrolyte was impaired (**Table 4**). Whereas m-PBI only experienced a volumetric electrolyte imbalance of 2.3 mL (5.8%) toward the negative electrode, Ethyl63 and Propyl60 exhibit an imbalance of 4.9 mL (12.3%) and 4.5 mL (11.3%), respectively. An explanation for the inconsistency between electrolyte imbalance and capacity fading can be found in the polymer packing of the dense polymer electrolyte, which changes from an ordered to a less ordered structure due to the addition of the small alkyl side chain, making the ionic domains less well-defined.[40] Furthermore, a molecular dynamics study by Hinkle et al. showed that vanadium ion transport required a pore size of 7 Å or larger in a zeolite membrane due to the strong binding of the hydration shell to the vanadium ion. This required size is larger than the correlation lengths observed in the dry functionalized m-PBI polymers (Figure 7), respectively, 4.2–6.7 Å. Although the correlation length will increase upon electrolyte uptake, the broad range of correlation lengths is likely to introduce a significant size-exclusion contribution. Therefore, the transport of the hydrated vanadium ions will be less affected by the alkylation than the transport of the H^+, HSO_4^-, and H_2O species in the electrolyte due to their smaller radius.[45]

The electrolyte crossover observed for the N-alkylated m-PBI derivatives is comparable to that of cells equipped with Nafion™ NR212, yet in opposite direction, owing to the stronger Donnan exclusion of the anolyte versus the catholyte as a result of its higher average charge.[16] The more balanced electrolyte crossover and capacity loss of the m-PBI materials suggest only small changes in the vanadium concentration during cycling, which is not the case for Nafion™ membranes.[46] As a consequence, PBI-based systems allow for continuous operation using a reflow mode, where the electrolyte tanks are connected through a capillary that enables continuous rebalancing and a constant electrolyte volume.[13] In contrast, Nafion™-based systems require periodic electrolyte remixing due to the changing electrolyte concentration, thereby showing the promise of PBI-based materials for usage in next-generation VRFBs.

Although the most promising cell characteristics were obtained for Ethyl63, with both the highest energy efficiency and capacity retention, it has to be stated that these membranes showed lower oxidative stability in the VO_2^+ accelerated stress test (Figure 8). A consideration must be made by the end user if the improved cell performance of this material is sufficient to warrant its use due to its expected lower lifetime. Nevertheless, a complete improvement to m-PBI can be found in Propyl60, with this derivative having comparable oxidative stability and capacity retention while maintaining a higher energy efficiency, thereby showing that cell performance can be improved without adversely affecting other relevant membrane properties.

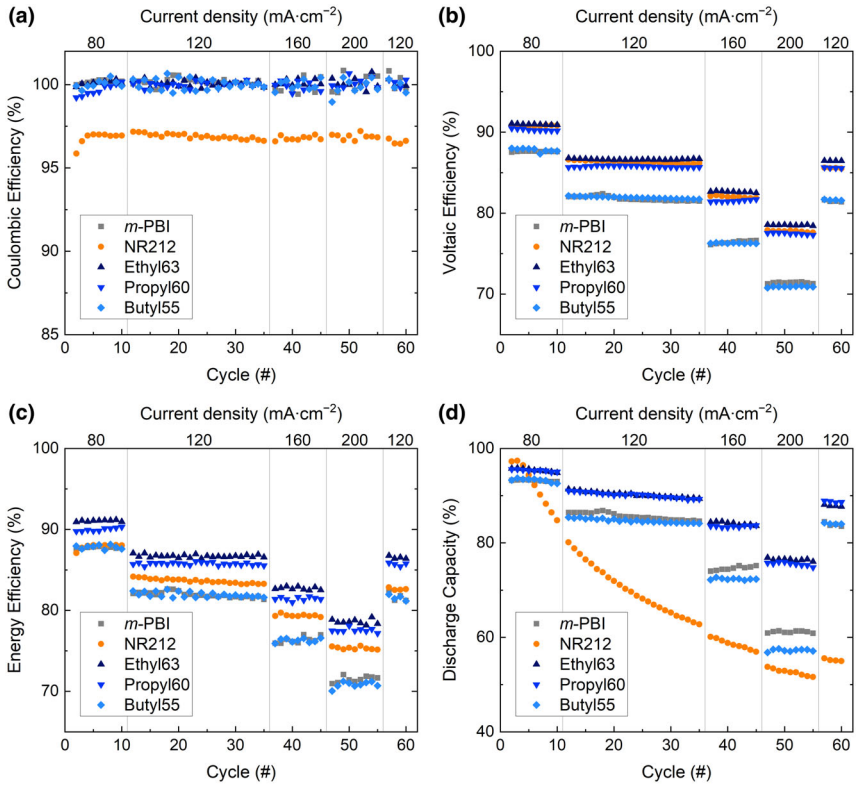

Figure 10. a) Coulombic efficiency, b) Voltaic efficiency, c) Energy efficiency, and d) Discharge capacity of single cells with *m*-PBI, Ethyl63, Propyl60, Butyl55, and Nafion™ NR212 at current densities between 80 and 200 mA cm^{-2}.

3. Conclusion

Novel low-cost and fluorine-free hydrocarbon membranes based on N-alkylated and N-benzylated m-PBI were analyzed for flow battery applications. Whereas benzylation triggers a stronger polymer chain interaction, decreasing its properties for VRFBs, N-alkylation results in a more disordered polymer packing, thereby increasing the electrolyte uptake and ionic conductivity of the polymer electrolyte and, consequently, its performance in the VRFB cell. The beneficial features in terms of acid uptake, thickness swelling, and ionic conductivity decreased with increasing length of the alkyl chain, attributed to the formation of hydrophobic regions inside the membrane, limiting the incorporation of charged protons and vanadium species. Partially alkylated m-PBI derivatives, Ethyl63, and Propyl60, outperformed pristine m-PBI and Nafion™ NR212 over 200 cycles at 200 mA cm^{-2}, with a respective average energy efficiency of ∼78% and ∼76% versus ∼70% and ∼75%. Although the ethylated and propylated derivatives saw an increase in the ex situ VO^{2+} diffusion versus pristine m-PBI, a similar increase in the in situ capacity fading was not observed. The excellent cycling features of the N-alkylated m-PBI polymer electrolytes at high current densities make this class of materials a promising candidate for next-generation flow battery membranes. Furthermore, the fundamental insight on the membrane's molecular design requirements, gained from the introduction of various alkyl and benzyl side chains on the properties of the polymer electrolyte can easily be applied to other fields of membrane research, thereby assisting in their search for next-generation membranes and consequently, working toward a global society based on renewable energy technologies.

4. Experimental Methods

Synthesis of functionalized PBI: Prior to each synthesis, *m*-PBI (BASF) was dried at 70 °C *in vacuo* overnight. After drying, the *m*-PBI polymer was placed under nitrogen using a Schlenk line and dissolved in dry *N,N,*-dimethylacetamide (Sigma Aldrich, Germany, 4 wt.%, DMAc) at 80 °C. The dissolved *m*-PBI was cooled to 40 °C and sodium hydride (NaH, Sigma-Aldrich) was added. The mixture was left to react overnight at 80 °C with a nitrogen purge to avoid the build-up of hydrogen. Upon cooling down to 40 °C, a slight excess of the halogenated side chain reagent was added, and the mixture was left to react for another 24 h. The exact conditions of each functionalization can be found in the Table S1, Supporting Information. After completion, the functionalized material was precipitated in acetone, collected through vacuum filtration, and washed with acetone (3 times). Subsequently, the material was dried at 70 °C *in vacuo* overnight and at 150 °C for 3 h. The functionalized PBI was obtained as a light brown powder, with the chemical structure being determined through ^{1}H NMR and ^{19}F NMR in DMSO-d_6.

The degree of functionalization (DoF) of the PBI derivatives was determined through the integration of the signals of the *m*-PBI backbone and the newly formed signals of the attached side chain. Hereby, the ratio between the aromatic signals (10 protons) and the end group of the alkyl chains was taken to determine the degree of functionalization for alkylated materials (Equation 1). In the case of benzylated compounds, the ratio between the CH_2 alkyl group and the aromatic signals was used to calculate the degree of functionalization (Equations 2–4). Herein, x is the number of attached chains per repeating unit and H_{ring} the amount of hydrogen atoms in the attached aromatic ring, respectively, 5 and 4 for BenzylX and FBenzylX. The value of x was obtained by iteratively solving Equations 2 and 3 through agreement. Subsequently, the DoF of the benzylated material could be calculated according to Equation 4.

$$\mathrm{DoF_{Alkylated}} = \frac{\mathrm{CH_3\ signal}}{6} \cdot 100 \quad (1)$$

$$\mathrm{Signal_{aromatic}} = 10 + \mathrm{H_{ring}x} \quad (2)$$

$$\mathrm{Signal_{CH_2}} = 2\mathrm{x} \quad (3)$$

$$\mathrm{DoF_{Benzylated}} = \frac{\mathrm{CH_2\ signal}}{4} \cdot 100 \quad (4)$$

Membrane preparation: Casting solutions consisting of 15 wt.% of *m*-PBI in dry DMAc were prepared through the dissolution of the polymer overnight at 80 °C. For the functionalized materials, a casting solution with a molar concentration equivalent to that of the 15 wt.% *m*-PBI was used.

Membranes were cast on a glass plate using applicators with a fixed blade gap of 150, 200, and 250 µm. DMAc was evaporated in an oven at 140 °C for 3 h. The thickness of the membrane was assessed with a profilometer (Dektak 8 Advanced Development Profiler, Veeco, USA), where six data points were taken to obtain the average thickness of the membrane. Membranes were separated from the glass plate through submersion in DI water. Subsequently, the membranes were placed in 2 M H_2SO_4 for direct use or dried in a vacuum oven at 70 °C *in vacuo* for 5 h and stored in a plastic zip-lock bag for future use.

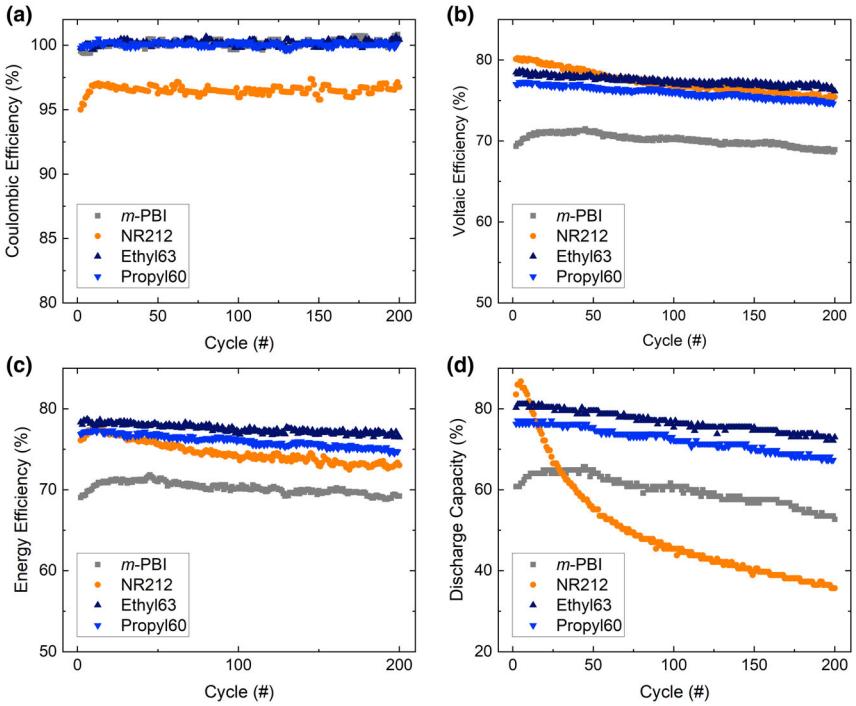

Figure 11. a) The coulombic efficiency, b) voltaic efficiency, c) energy efficiency, and d) discharge capacity of *m*-PBI, Ethyl63, Propyl60, and Nafion™ NR212 over 200 cycles at 200 mA cm^{-2}. The coulombic efficiency was averaged with a 5 point moving average (2 before, 2 after) to minimize the influence of software related data collection deviations. Five cycles were omitted from the Propyl60 as a result of a software error.

Thickness swelling and acid uptake: The acid uptake and thickness swelling of pristine and functionalized PBI were determined through the analysis of four samples (4.0 × 2.0 cm). The dry weight, m_{dry}, and thickness, t_{dry}, of the membrane were measured after drying at 70 °C *in vacuo* for 20 h. Here, the dry weight of the film was measured inside a closed glass vial with a known weight to avoid the imbibition of moisture from the air into the film. The swollen thickness, t_{wet}, of the membrane was measured after immersion in 2 M H_2SO_4 for 24 h. Subsequently, the membranes were immersed for another 24 h in 2 M H_2SO_4 to avoid the drying of the films during the thickness measurements. Afterward, the wet weight, m_{wet}, was determined inside a closed glass vial with a known weight to avoid the drying of the films. The dried weight of the film, m_{dried}, was measured after drying the membrane and the glass vial used in the m_{wet} measurements at 70 °C *in vacuo*. After 24 h, the glass vial with its corresponding film was removed from the vacuum oven and immediately closed to avoid the imbibition of water. The closed vials were allowed to cool down to room temperature, after which they were opened for 5 s to remove the pressure (and mass) difference formed due to a decrease in air density inside the vial. The thickness swelling and mass uptake were calculated according to Equations 5–8. The acid doping level was calculated using Equation 9, with n_{H2SO4} and n_{PBI} calculated from the H_2SO_4 uptake and m_{dry}, respectively.

$$\text{Thickness swelling} = \frac{t_{wet} - t_{dry}}{t_{dry}} \quad (5)$$

$$\text{Mass uptake} = \frac{m_{wet} - m_{dry}}{m_{dry}} \quad (6)$$

$$H_2SO_4 \text{ uptake} = \frac{m_{dried} - m_{dry}}{m_{dry}} \quad (7)$$

$$H_2O \text{ uptake} = \text{Mass uptake} - H_2SO_4 \text{ uptake} \quad (8)$$

$$\text{Acid doping level} = \frac{n_{H_2SO_4}}{n_{PBI}} \quad (9)$$

Ionic conductivity: The ionic conductivity of pristine and functionalized *m*-PBI as well as Nafion™ NR212 in 2 M H_2SO_4 and the vanadium electrolyte (oxidation state 3.5; Oxkem, UK) was determined in a through-plane conductivity cell equipped with platinum electrodes (Figure S13, Supporting Information). All membranes were immersed in 2 M H_2SO_4 or the vanadium electrolyte for 24 h prior to testing, with NR212 being equilibrated in DI water before immersion into the respective electrolyte solution. The membrane, 2 cm diameter, was placed inside the conductivity cell, and the electrolyte was injected. The cell was repeatedly flushed with electrolyte to remove air bubbles from the system. The high-frequency resistance was recorded using electrochemical impedance spectroscopy (EIS) between 1 MHz and 50 kHz with a biologic SP-300 (Biologic, France). The membrane resistance was obtained from the cell resistance through the stacking of 1–5 films. The obtained slope hereby corresponds to the membrane resistance, with the *y*-intercept being the cell resistance. The ionic conductivity of the membrane was calculated according to Equation 10, with *t* as the measured swollen thickness of the membrane in cm, Ω_{mem} the membrane resistance, and $A_{electrode}$ the area of the electrode, respectively 1.77 cm^2.

$$\sigma = \frac{t}{\Omega_{mem} \cdot A_{electrode}} \quad (10)$$

Mechanical strength: The mechanical properties of pristine and functionalized *m*-PBI membranes were assessed in an acid-swollen state at room temperature with a Z005 (ZwickRoell, Germany) testing device following an ASTM D 882 protocol. Nafion™ N117 and NR212 were used as commercial references.

For each membrane, ten strips (10.0 × 1.0 cm) were prepared from a 2 M H_2SO_4 preswollen membrane sheet and stored in 2 M H_2SO_4. Samples were assembled with an initial grip-to-grip separation of 5.0 cm and were preloaded to 1 MPa at a speed of 10 mm min^{-1}. Subsequently, the testing occurred at a speed of 500 mm min^{-1} until breakage.

Measurements showing a break in the initial stage of the experiment were excluded from the data set, with the mean of the remainder of the data set being reported in Figure 4.

VO^{2+} diffusion: The VO^{2+} diffusivity through NR212, pristine, and functionalized *m*-PBI was determined in an ex situ VO^{2+} diffusivity test. The PBI-type membranes were preswollen in 2 M H_2SO_4, with NR212 being preswollen in DI water. The swollen membrane (3.6 cm diameter) was placed in a home-built diffusion cell (Figure S16, Supporting Information) between a VO^{2+} donating compartment (1.6 M $VOSO_4$ in 2 M H_2SO_4, 80 mL) and a receiving compartment (1.6 M $MgSO_4$ in 2 M H_2SO_4, 80 mL). Both solutions were continuously stirred to ensure homogeneous mixing. Samples of the receiving compartment were taken for UV-Vis spectroscopy (Cary 4000; Agilent, USA) at regular intervals. Each measurement was carried out by filling a quartz cuvette (1.0 cm, Hellma Analytics, Switzerland) with 2.5 mL of the VO^{2+}-deficient compartment, after which the light absorbance was recorded between a wavelength of 500 and 800 nm. The absorbance peak of $VOSO_4$ at 765 nm was used to calculate the VO^{2+} concentration according to a determined measured calibration curve (Figure S15, Supporting Information). After the measurement, the analyzed solution was inserted back into the corresponding VO^{2+} receiving compartment to avoid volume imbalances. Due to the high VO^{2+} diffusivity through NR212, samples were diluted 10 times after day 2 to avoid the absorbance exceeding 1. The $VOSO_4$ diffusion coefficient of the respective membrane (D_{VOSO4}) was calculated according to a modified Fick's law, Equation 11.[25]

Table 4. Capacity retention, capacity loss, with respect to the starting capacity and theoretical capacity, and imbalance formation of *m*-PBI, Nafion™ NR212, Ethyl63, and Propyl60 after 200 cycles at 200 mA cm^{-2} (Figure 11).

Membrane	Capacity retention (%)	Absolute capacity loss (%)	Imbalance (mL)	Imbalance (%)	Imbalance direction
m-PBI	87	8.1	2.3	5.6	–
NR212	43	47.8	4.5	11.3	+
Ethyl63	91	7.3	4.9	12.1	–
Propyl60	88	8.9	4.5	11.3	–

$$V_r \cdot \frac{d(C_r(t))}{dt} = A \cdot \frac{D_{VOSO_4}}{t} \cdot (C_d - C_r(t)) \quad (11)$$

Herein, V_r is the volume of the VO^{2+} receiving compartment (80 mL), A is the area of the membrane (10.2 cm^2), t is the thickness of the swollen membrane in cm, C_d is the VO^{2+} concentration in the donating compartment, and C_r the measured VO^{2+} concentration in the receiving compartment at a given time, obtained from a linear regression of the measured concentrations.

Structural analysis: The nanostructure of pristine and functionalized *m*-PBI was analyzed using small-angle X-ray scattering (SAXS) and wide-angle X-ray scattering (WAXS). Prior to the SAXS analysis, *m*-PBI and functionalized *m*-PBI films with a dry thickness of ~20 µm were equilibrated in 2 M H_2SO_4 for 24 h. SAXS experiments were carried out on a benchtop Bruker Nanostar (Bruker AXS GmbH, Karlsruhe, Germany) using the K_α-line of a micro-focused X-ray Cu source with a wavelength of 1.5406 Å. The beam was collimated using a 0.3 mm pinhole, leading to a beam diameter of approximately 0.4 mm at the sample position. The sample-detector distance was set to 107 and 13 cm and further calibrated with silver behenate, achieving a resolvable q-range of $0.07 \leq q \leq 20.8\ nm^{-1}$. The scattering vector q is defined as depicted in Equation 12, with 2Θ as the scattering angle and λ, the wavelength of the X-ray source recorded on a gaseous avalanche-based detector (VÅNTEC-2000, Bruker AXS) with 2048 × 2048 pixels and a pixel size of 68 × 68 μm^2. The scattering patterns were recorded at room temperature under moderate vacuum conditions (10^{-2} mbar) to limit air scattering.

$$\overrightarrow{|q|} = (4\pi/\lambda)\sin\left(\frac{2\theta}{2}\right) \quad (12)$$

The calibration of the scattering vector q and the estimation of the instrumental resolution of $\Delta q = 0.25\ nm^{-1}$ were done by measuring the first diffraction peak of a silver behenate sample and calculating its width. Each sample was sealed in a quartz capillary (1.5 mm, Heidenberg GmbH, Germany) with 2 M H_2SO_4 electrolyte and mounted in the sample chamber. Scattering was recorded for 6 h in transmission mode for each sample and background. The intensity of the semi-transparent beamstop for direct beam scans was used for transmission normalization. The scattered intensity was extracted, azimuthally averaged, and integrated over each q-value using the Bruker software DIFFRAC.EVA (Bruker AXS, version 4.1). The 1D data was transmission corrected and background-subtracted from the scattering of the respective solvents, polymers, and the empty quartz capillary using an in-house data pipeline operating under Matlab 2022.

The WAXS measurements were conducted in an IPDS-II diffractometer (STOE & Cie) using a Mo K_α radiation source with a wavelength of 0.7107 Å. Here, the dry *m*-PBI and functionalized *m*-PBI films (~20 µm dry thickness) were rolled up and partly placed into a goniometer sample holder, allowing us to measure all samples without a container. The WAXS patterns of the PBI films were recorded in transmission mode, with a 200 mm detector distance from the sample and a 10 rpm rotation for 2–4 h. The obtained WAXS patterns were converted from Mo K_α radiation to Cu K_α radiation for graphic presentation (Figure 7) and for comparison with related published work.

Chemical stability: The oxidative stability of pristine and alkylated *m*-PBI was assessed in a 1.6 M VO_2^+ electrolyte solution. The V(V) electrolyte solution was obtained by the complete oxidization of a commercial 1.6 M vanadium electrolyte in 2 M H_2SO_4 and 0.05 M H_3PO_4 (average oxidation state 3.5; Oxkem, UK) in a VRFB setup equipped with a Nafion™ NR212 membrane. Here, a slight excess of electrolyte was added to the negative compartment to ensure complete oxidation of the positive electrolyte. The electrolyte was galvanostatically charged at 80 mA cm^{-2} until the voltage cut-off limit of 1.8 V was reached. Subsequently, the cell was potentiostatically charged at a voltage of 2.2 V until the lower current limit of 20 mA cm^{-2} was reached. The positive electrolyte was then extracted to be used in the oxidative stability test. Pristine and functionalized *m*-PBI (50–80 mg) were added to a glass vial and immersed in 4.5 mL of V(V) electrolyte. Before closing, the vials were flushed with nitrogen to limit the influence of oxygen. The vials were opened after 21, 42, and 66 days to determine the extent of VO^{2+} formation, through the oxidation of the membrane. Hereby, 100 µL of the to be analyzed V(V) catholyte was diluted with 4.9 mL of 2 M H_2SO_4. Subsequently, the VO^{2+} concentration was determined through UV-Vis spectroscopy. A reference solution of the added V(V) electrolyte, stored away for the same period, was used as a baseline to determine VO^{2+} concentration increase, measured at a wavelength of 765 nm. The VO^{2+} formation over time was normalized according to the weight of the added polymer.

After 66 days, the membranes were washed in DI water, dried overnight at 70 °C *in vacuo* and subsequently analyzed with FTIR spectroscopy (Vertex V70 spectrometer; Bruker, USA) between 400 and 4000 cm^{-1}.

Cell cycling: Pristine and functionalized *m*-PBI were characterized for their VRFB cell cycling performance in an electrochemical test station (Scribner Model 857 test stand; Scribner Associates, USA) at a dry thickness of 12–15 µm, with Nafion™ NR212 (51 µm dry thickness; Ion Power, USA) being used as the commercial reference. The electrochemical test station was equipped with a 25 cm^2 laboratory electrochemical cell (Scribner Associates, USA) that was connected to two in-house designed graduated cylindrical glass electrolyte tanks and a multichannel peristaltic pump (Masterflex L/S®, GZ-07522–20; Cole-Parmer GmbH, Germany) with plasticizer-free chemical-resistant tubing (Versilon™ 2001; GZ-06475-16, Cole-Parmer GmbH, Germany). The assembly of the electrochemical cell consisted of 1) two gold-plated copper current collectors (Scribner Associates, USA), 2) two triple-serpentine-cured furan resin graphite flow fields (Fuel Cell Technologies, Inc., USA), 3) two in-house designed polyvinylidene fluoride gasket frames (2.5 mm thickness) equipped with two ice cube gaskets (0.8 mm, 35 FC-PO100, Germany) for sealing purposes, and 4) two pretreated carbon felt electrodes (25 cm^2 active area, AAF304ZS, Toyobo, Japan), used as received. The electrochemical cell was tightened to 4 N m, corresponding to a compression of 42% of the carbon electrodes. The vanadium electrolyte (1.6 M vanadium in 2 M H_2SO_4 and 0.05 M H_3PO_4, oxidation state 3.5, Oxkem, UK) was circulated between the electrochemical cell and the electrolyte tanks at 60 mL min^{-1}, with both electrolyte tanks being filled with 40 mL of vanadium electrolyte at the start of the test. The oxidation of the electrolyte due to the presence of oxygen was avoided by continuously flushing both electrolyte tanks with argon (66 mL min^{-1}).

Prior to cell assembly, Nafion™ NR212 and pristine and functionalized *m*-PBI were preswollen in DI water and 2 M H_2SO_4 overnight, respectively, to enhance their cycling performance.

The cycling performance of all membranes was screened using a galvanostatic cycling protocol at varying current densities. The cycling protocol consisted of three phases, 1) a 4 h conditioning step at OCV, followed by an electrochemical impedance spectroscopy measurement between 10 kHz and 0.1 Hz at zero DC and a perturbation amplitude of 10 mV to determine the high-frequency resistance (HFR); 2) the initial charging step of the electrolyte at 40 mA cm^{-2}, using 1.65 V as the upper cut-off limit, with polarization curves recorded at a state of charge of 20%, 30%, 50%, 70%, and 90%, by consecutively charging and discharging the electrolyte at 20, 40, 60, 80, 120, 150, and 200 mA cm^{-2} for 20 s. The last phase; and 3), was the VRFB cell cycling at varying current densities. Here, the system was sequentially galvanostatically cycled between 0.80 and 1.65 V at a current density of 80, 120, 160, 200, and 120 mA cm^{-2} for, respectively, 10, 25, 10, 10, and 5 cycles. The 1st cycle at each current density was omitted due to the influence of the prior current density.

The well-performing membranes were further characterized in an extended cycling test of 200 cycles at 200 mA cm^{-2}. As before, the preswollen membranes were conditioned for 4 h at OCV before measuring their HFR between

10 kHz and 0.1 Hz at zero DC and a perturbation amplitude of 10 mV. Subsequently, the test station was charged to 1.65 V at 200 mA cm^{-2}, before starting the cycling protocol of 200 cycles at 200 mA cm^{-2}, with 0.80 and 1.65 V as the lower and upper cut-off limits. A moving average of 5 cycles, respectively, the current cycle with two cycles prior and after, was used to reduce the variance of the coulombic efficiency, in addition to the 1st cycle of the test being omitted.

The membrane performance during the VRFB cycling was assessed through the cycling efficiencies (CE, VE, and EE) and the normalized discharge capacity (Q_d), calculated according to Equations 13–16. Herein, t_d and t_c indicate the discharging and charging time of the cycle, $\overline{U}_d$ and $\overline{U}_c$ the average voltage during discharging and charging, $Q_{d,abs}$ the measured discharge capacity, n the number of moles of the electroactive vanadium species, F the Faraday constant (96 485 C mol^{-1}) and z the number of electrons associated with the electrochemical reaction (1).

$$\text{Coulombic efficiency, CE}\ (\%, \text{constant } i) = \frac{t_d}{t_c} \cdot 100\% \tag{13}$$

$$\text{Voltaic efficiency, VE}\ (\%) = \frac{\overline{U}_d}{\overline{U}_c} \cdot 100\% \tag{14}$$

$$\text{Energy efficiency, EE}\ (\%) = \text{CE} \cdot \text{VE} \tag{15}$$

$$Q_d\ (\%) = \frac{Q_{d,abs}}{Q_{theo}} = \frac{Q_{d,abs}}{I \cdot t} = \frac{Q_{d,abs}}{n \cdot F \cdot z} \cdot 100\% \tag{16}$$

Acknowledgements

The authors acknowledge A. Schneider (PSI) for his contribution and assistance to the project. The research at the Paul Scherrer Institute is supported by the Swiss National Science Foundation (grant number 188631).

Conflict of Interest

The authors declare no conflict of interest.

Author Contributions

Conceptualization, JCD; Data curation, JCD, JA; Formal analysis, JCD, JA; Funding acquisition, LG; Investigation, JCD, JA, LK, and AN; Methodology, JCD; Project administration, LG; Resources, AN, LG; Supervision, BFBS, AN, TJS, and LG; Validation, JCD; Visualization, JCD; Writing—original draft, JCD, JA; Writing—review and editing, JCD, JA, LK, BFBS, AN, TJS, and LG.

Supporting Information

Supporting Information is available from the Wiley Online Library or from the author.

Keywords

design principles, energy storage devices, membranes, polybenzimidazole, vanadium redox flow batteries

Received: March 7, 2024
Revised: May 3, 2024
Published online: May 23, 2024

[1] B. R. Chalamala, T. Soundappan, G. R. Fisher, M. R. Anstey, V. V. Viswanathan, M. L. Perry, *Proc. IEEE* **2014**, *102*, 976.
[2] M. Skyllas-Kazacos, M. H. Chakrabarti, S. A. Hajimolana, F. S. Mjalli, M. Saleem, *J. Electrochem. Soc.* **2011**, *158*, R55.
[3] M. C. Argyrou, P. Christodoulides, S. A. Kalogirou, *Renew. Sust. Energ. Rev.* **2018**, *94*, 804.
[4] L. F. Arenas, F. C. Walsh, C. P. de León, *Flow Batteries* (Eds: C. Roth, J. Noack, M. Skyllas-Kazacos), Wiley-VCH, Weinheim, Germany **2023**, Ch. 4.
[5] D. G. Kwabi, Y. Ji, M. J. Aziz, *Chem. Rev.* **2020**, *120*, 6467.
[6] S. Gentil, D. Reynard, H. H. Girault, *Curr. Opin. Electrochem.* **2020**, *21*, 7.
[7] C. Sun, H. Zhang, *ChemSusChem* **2022**, *15*, e202101798.
[8] Y. A. Hugo, W. Kout, G. Dalessi, A. Forner-Cuenca, Z. Borneman, K. Nijmeijer, *PRO* **2020**, *8*, 1492.
[9] J. Noack, N. Roznyatovskaya, T. Herr, P. Fischer, *Angew. Chem. Int. Ed.* **2015**, *54*, 9776.
[10] Y. Shi, C. Eze, B. Xiong, W. He, H. Zhang, T. M. Lim, A. Ukil, J. Zhao, *Appl. Energy* **2019**, *238*, 202.
[11] G. Kear, A. A. Shah, F. C. Walsh, *Int. J. Energy Res.* **2012**, *36*, 1105.
[12] H. Zhang, W. Lu, X. Li, *Electrochem. Energy Rev.* **2019**, *2*, 492.
[13] B. Bauer, T. Klicpera, K. Reinwald, M. Schuster, Ion Exchange Membranes for Energy Applications (EMEA) Workshop. **2018**.
[14] C. Minke, U. Kunz, T. Turek, *J. Power Sources* **2017**, *361*, 105.
[15] Y. Chen, P. Xiong, S. Xiao, Y. Zhu, S. Peng, G. He, *Energy Storage Mater.* **2022**, *45*, 595.
[16] F. J. Oldenburg, T. J. Schmidt, L. Gubler, *J. Power Sources* **2017**, *368*, 68.
[17] F. J. Oldenburg, E. Nilsson, T. J. Schmidt, L. Gubler, *ChemSusChem* **2019**, *12*, 2620.
[18] I. S. Chae, T. Luo, G. H. Moon, W. Ogieglo, Y. S. Kang, M. Wessling, *Adv. Energy Mater.* **2016**, *6*, 1600517.
[19] C. Noh, M. Jung, D. Henkensmeier, S. W. Nam, Y. Kwon, *ACS Appl. Mater. Interfaces* **2017**, *9*, 36799.
[20] S. Peng, X. Yan, X. Wu, D. Zhang, Y. Luo, L. Su, G. He, *RSC Adv.* **1852**, *2017*, 7.
[21] Y. H. Wan, J. Sun, H. R. Jiang, X. Z. Fan, T. S. Zhao, *J. Power Sources* **2021**, *489*, 229502.
[22] D. Aili, D. Henkensmeier, S. Martin, B. Singh, Y. Hu, J. O. Jensen, L. N. Cleemann, Q. Li, *Electrochem. Energy Rev.* **2020**, *3*, 793.
[23] J. Mader, L. Xiao, T. J. Schmidt, B. C. Benicewicz, in *Fuel Cells II* (Ed: G. G. Scherer), Springer Berlin Heidelberg, Berlin, Heidelberg **2008**, p. 63.
[24] A. T. Pingitore, M. Molleo, T. J. Schmidt, B. C. Benicewicz, in *Fuel Cells and Hydrogen Production: A Volume in the Encyclopedia of Sustainability Science and Technology*, 2nd ed. (Eds: T. E. Lipman, A. Z. Weber), Springer New York, New York, NY **2019**, p. 477.
[25] Z. Yuan, Y. Duan, H. Zhang, X. Li, H. Zhang, I. Vankelecom, *Energy Environ. Sci.* **2016**, *9*, 441.
[26] W. Lee, B. W. Kwon, M. Jung, D. Serhiichuk, D. Henkensmeier, Y. Kwon, *J. Power Sources* **2019**, *439*, 227079.
[27] C. Noh, D. Serhiichuk, N. Malikah, Y. Kwon, D. Henkensmeier, *Chem. Eng. J.* **2021**, *407*, 126574.
[28] D. Aili, J. Yang, K. Jankova, D. Henkensmeier, Q. Li, *J. Mater. Chem. A* **2020**, *8*, 12854.
[29] Q. Dai, F. Xing, X. Liu, D. Shi, C. Deng, Z. Zhao, X. Li, *Energy Environ. Sci.* **2022**, *15*, 1594.
[30] S. C. Kumbharkar, K. Li, *J. Membr. Sci.* **2012**, *415*, 793.
[31] M. Mara Ikhsan, S. Abbas, X. H. Do, S.-Y. Choi, K. Azizi, H. A. Hjuler, J. H. Jang, H. Y. Ha, D. Henkensmeier, *Chem. Eng. J.* **2022**, *435*, 134902.
[32] L. Wang, A. T. Pingitore, W. Xie, Z. Yang, M. L. Perry, B. C. Benicewicz, *J. Electrochem. Soc.* **2019**, *166*, A1449.
[33] L. Gubler, D. Vonlanthen, A. Schneider, F. J. Oldenburg, *J. Electrochem. Soc.* **2020**, *167*, 100502.
[34] J. C. Duburg, K. Azizi, S. Primdahl, H. A. Hjuler, E. Zanzola, T. J. Schmidt, L. Gubler, *Molecules* **2021**, *26*, 1679.
[35] P. Xiong, L. Zhang, Y. Chen, S. Peng, G. Yu, *Angew. Chem. Int. Ed.* **2021**, *60*, 24770.

[36] S. Peng, X. Wu, X. Yan, L. Gao, Y. Zhu, D. Zhang, J. Li, Q. Wang, G. He, *J. Mater. Chem. A* **2018**, *6*, 3895.
[37] B. Pang, X. Wu, Y. guo, M. Yang, R. Du, W. Chen, X. Yan, F. Cui, G. He, *J. Membr. Sci.* **2023**, *670*, 121351.
[38] A. G. Wright, J. Fan, B. Britton, T. Weissbach, H.-F. Lee, E. A. Kitching, T. J. Peckham, S. Holdcroft, *Energy Environ. Sci.* **2016**, *9*, 2130.
[39] X. Yan, Z. Dong, M. Di, L. Hu, C. Zhang, Y. Pan, N. Zhang, X. Jiang, X. Wu, J. Wang, G. He, *J. Membr. Sci.* **2020**, *596*, 117616.
[40] J.-K. Jang, S.-W. Jo, J. W. Jeon, B. G. Kim, S. J. Yoon, D. M. Yu, Y. T. Hong, H.-T. Kim, T.-H. Kim, *ACS Appl. Energy Mater.* **2021**, *4*, 4672.
[41] K. D. Kreuer, *J. Membr. Sci.* **2001**, *185*, 29.
[42] X. L. Zhou, T. S. Zhao, L. An, L. Wei, C. Zhang, *Electrochim. Acta* **2015**, *153*, 492.
[43] B. Pang, Q. Zhang, X. Yan, X. Wang, W. Chen, R. Du, X. Wu, M. Guo, G. He, F. Cui, *J. Power Sources* **2021**, *506*, 230203.
[44] R. Darling, K. Gallagher, W. Xie, L. Su, F. Brushett, *J. Electrochem. Soc.* **2016**, *163*, A5029.
[45] K. R. Hinkle, C. J. Jameson, S. Murad, *J. Phys. Chem. C* **2014**, *118*, 23803.
[46] Q. Luo, L. Li, W. Wang, Z. Nie, X. Wei, B. Li, B. Chen, Z. Yang, V. Sprenkle, *ChemSusChem* **2013**, *6*, 268.